In Vivo Quantitative Evaluation of the Transport Kinetics of Gold Nanocages in a Lymphatic System by Noninvasive Photoacoustic Tomography

Xin Cai,[†] Weiyang Li,[†] Chul-Hong Kim,[‡] Yuchen Yuan, Lihong V. Wang,[*] and Younan Xia[*]

Department of Biomedical Engineering, Washington University in St. Louis, St. Louis, Missouri 63130, United States. [‡]Present address: Department of Biomedical Engineering, The State University of New York, Buffalo, New York 14260, Unites States. [†]These two authors contributed equally to this work.

ABSTRACT

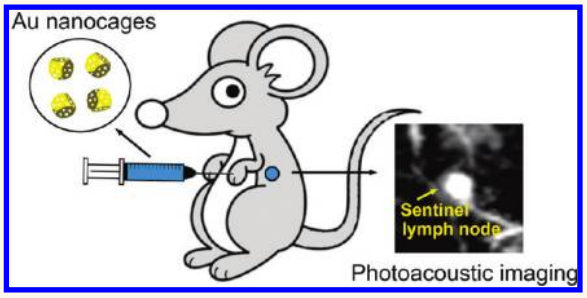

Sentinel lymph node (SLN) biopsy has emerged as a preferred method for axillary lymph node staging of breast cancer, and imaging the SLN in three-dimensional space is a prerequisite for the biopsy. Conventional SLN mapping techniques based on the injection of an organic dye or a suspension of radioactive colloids suffer from invasive surgical operation for visual detection of the dye or hazardous radioactive components and low spatial resolution of Geiger counters in detecting the radioactive colloids. This work systematically investigates the use of gold nanocages (AuNCs) as a novel class of optical tracers for noninvasive SLN imaging by photoacoustic (PA) tomography in a rat model. The transport of AuNCs in a lymphatic system and uptake by the SLN were evaluated by PA tomography on the axillary region of a rat. Quantification of AuNCs accumulated in the lymph node was achieved by correlating the data from PA imaging with the results from inductively coupled plasma mass spectrometry. Several parameters were systematically evaluated and optimized, including the concentration, size, and surface charge of the AuNCs. These results are critical to the further development of this AuNC-based PA tomography system for noninvasive SLN imaging, providing valuable information for metastatic cancer staging.

KEYWORDS: gold nanocages · sentinel lymph node · photoacoustic tomography · metastatic cancer staging

The metastatic spread of a tumor occurs by invading the adjacent tissue and disseminating cancerous cells through the lymphatic system into the bloodstream.[1] The closest lymph node that receives the drainage from a tumor is known as the sentinel lymph node (SLN), which represents the most likely first location of metastatic spread. To reduce the side effects of axillary lymph node dissection,[2] sentinel lymph node biopsy (SLNB) is widely performed and has become the standard for axillary staging in breast cancer patients.[3] Although SLNB with blue dyes (such as lymphazurin or methylene blue) or radioactive colloidal tracers has an identification rate of more than 90%, these methods involve invasive surgical operations and use carcinogenic ionizing radiation. They may also fail to identify axillary diseases owing to a high false negative rate of 5−10%.[4] Furthermore, they can pose a risk of postoperative complications, such as seroma formation, lymphedema, and motion limitation.[5]

Recently, ultrasound-guided fine needle aspiration biopsy (FNAB) has been clinically evaluated as a minimally invasive procedure.[6] This technique requires accurate positioning of the SLN, which initiates studies to develop accurate, nonionizing, and noninvasive methods for SLN mapping. Photoacoustic (PA) tomography is such a technique with remarkable resolution, which is based on the optical absorption contrast mechanism.[7,8] Since the spatial resolution of this technique is determined by ultrasound parameters, the imaging depth can be extended to the optical quasidiffusive or diffusive regime while maintaining high resolution. By using diffusive photons, the maximum PA imaging depth can be pushed up to 50 mm in biological tissues.[9] Our previous work successfully demonstrated PA SLN imaging by using clinically available organic dyes.[10,11] Although this dye-based PA imaging system has been demonstrated with a depth capability of ∼31 mm, satisfactory spatial resolution, and clinical potential, the drawback of this system is

* Address correspondence to xia@biomed.wustl.edu, lhwang@biomed.wustl.edu

Received for review August 15, 2011 and accepted November 4, 2011.

Published online November 04, 2011
10.1021/nn203124x

that the dye molecules are rather small (<2 nm), and thus they can easily transport into the echelon lymph nodes, causing a high possibility of false positives.[12]

In contrast, gold nanocages (AuNCs), a novel class of nanostructures characterized by hollow interiors and ultrathin, porous walls, have a proper size range (30−100 nm) to ensure sufficiently fast migration and sufficient duration of trapping in SLN for imaging.[8] The localized surface plasmon resonance (LSPR) peak of AuNCs can also be precisely tuned to the near-infrared (NIR) region from 700 to 900 nm (the so-called transparent window), in which the attenuation of light by blood and soft tissue is relatively low.[13] In addition, AuNCs can be easily bioconjugated with various types of ligands such as antibodies, peptides, and nucleic acids to target specific receptors,[14,15] potentially eliminating the need for invasive axillary staging procedures in addition to providing noninvasive SLN mapping. Other attractive features of AuNCs include bioinertness, large absorption cross sections (almost 5 orders of magnitude greater than those of conventional organic dyes),[16] and the ability to encapsulate therapeutic drugs, which offers a great benefit for theranostic applications.[17] In a previous publication, we have demonstrated a proof-of-concept use of AuNCs for SLN imaging by PA tomography, where an intradermal injection of 100 μL of 2 nM AuNC solution was performed on the forepaw pad of a rat, and the SLN was identified with enhanced contrast and good spatial resolution.[18] Many parameters associated with the AuNCs, including the minimum requirement on the concentration and injected volume and the influence of particle size, shape, and surface characteristics on their transport kinetics and uptakes by lymph nodes, still need to be examined and optimized before this system can be further considered for potential clinical use.

Here we quantitatively evaluated the transport of AuNCs in the lymphatic system and the uptake by lymph nodes through PA imaging on a rat model. The influences of concentration, particle size, and surface charge were all systematically examined. The amounts of AuNCs accumulated in the SLNs were quantified by inductively coupled plasma mass spectrometry (ICP-MS) analysis of the dissected lymph nodes after the rats had been euthanized. The results provide valuable information for further development of this AuNC-based PA imaging system for noninvasive lymph node mapping.

RESULTS AND DISCUSSION

The main objective of this study is to quantitatively investigate the PA contrast enhancement in SLNs provided by AuNCs with different concentrations, sizes, and surface characteristics. The influences of these parameters were examined by using suspensions of AuNCs with a range of concentrations, two different sizes (50 and 30 nm in edge length), and three different surface charges (negative, positive, and neutral). Figure 1, A and B, shows typical transmission electron microscopy (TEM) images of AuNCs with an edge length of 50 and 30 nm, respectively. Figure 1C shows the UV−vis extinction spectra of 50 and 30 nm AuNCs. The locations of their LSPR peaks were slightly different, centered at 760 and 730 nm, respectively. During PA imaging, the laser wavelength was tuned to overlap with the corresponding absorption peak. Except for the experiments involving comparison of particle size, the AuNCs used in all studies were 50 nm in edge length.

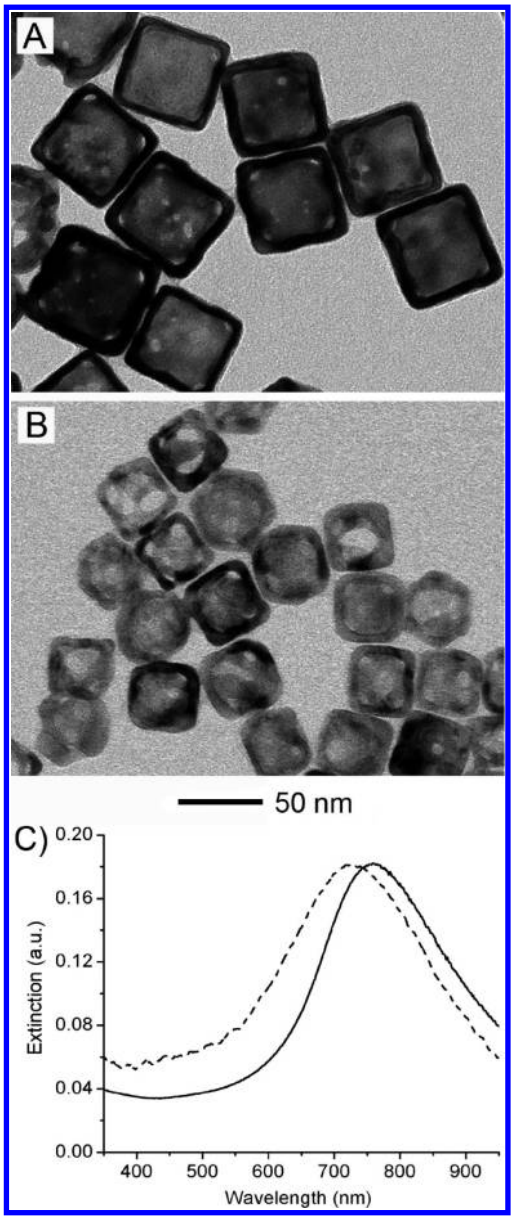

Figure 1. TEM images of Au nanocages (AuNCs) with average edge lengths of (A) 50 nm and (B) 30 nm; (C) UV−vis extinction spectra of aqueous suspensions of AuNCs with edge lengths of 50 nm (solid line) and 30 nm (dashed line).

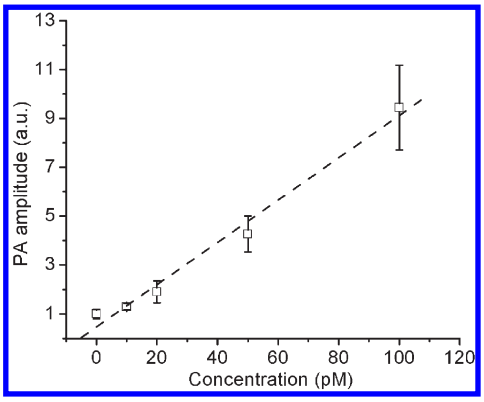

Figure 2. PA signals recorded from gelatin phantoms containing AuNCs at various concentrations (R^2 = 0.99), showing that the detection limit of AuNCs (50 nm in edge length) was less than 10 pM, or 2×10^5 (or 3.3×10^{-19} mol) AuNCs per imaging voxel, for the PA system. If we assume the typical volume of the SLN in a rat is ~23.6 mm^3 (the SLN is approximated as an ellipsoid of 3 mm × 5 mm × 3 mm), this detection sensitivity indicates that only ~1.3×10^8 (or 2.1×10^{-16} mol) AuNCs need to enter the lymph node to provide sufficient signals for imaging.

The surface of the as-synthesized AuNCs is typically covered with poly(vinyl pyrrolidone) (PVP, MW ≈ 55 000), a biocompatible polymer. To investigate the effect of surface charges, the PVP layer was replaced by heterofunctional poly(ethylene glycol) (PEG, MW ≈ 5000) with one end terminated in the sulfhydryl group and the other terminated by the amine (−NH_2), methoxy (−OMe), or carboxylic acid (−COOH) group, to generate positive, neutral, or negative surface charges, respectively. The as-prepared AuNCs covered by PVP were used in all experiments except the study of surface charges. The injection volume was kept the same at 100 μL for all experiments, while the concentration of AuNCs was varied. PA imaging of the axillary region of a Sprague−Dawley rat (250−300 g) was performed at different time points after intradermal injection of an aqueous suspension of AuNCs in the left forepaw pad, and the amplitude change of PA signals was then monitored as a function of time.

We first tested the *ex vivo* sensitivity of our current deep-reflection mode PA imaging system by using gelatin phantoms based on a mixture of gelatin and AuNCs.[18,19] As shown in Figure 2, PA signals from the gelatin phantom containing AuNCs at a concentration as low as 10 pM could still be detected with a signal-to-noise ratio (SNR) of ~2.2 dB. This detection limit corresponds to ~2×10^5 (or 3.3×10^{-19} mol) AuNCs per imaging voxel. If we assume the typical volume of SLN in a rat is ~23.6 mm^3 (the SLN is approximated as an ellipsoid of 3 mm × 5 mm × 3 mm), this detection sensitivity indicates that only ~1.3×10^8 (or 2.1×10^{-16} mol) AuNCs need to enter the lymph node to provide sufficient signals for imaging. The noise equivalent concentration (*i.e.*, the concentration that provides a SNR of unity) is calculated to be ~4.5 pM. In addition, the *ex vivo* experiment showed that no structural change to the nanocages was observed after expossure to the laser (determined by the TEM image), indicating that the nanocages were stable during the PA imaging. The power density of the laser applied was 35 mW/cm^2 and was kept at this level for all the *in vivo* studies.

To evaluate the *in vivo* sensitivity of our PA system and AuNCs for lymph node imaging, we intradermally injected an aqueous suspension of AuNCs at a specific, decreasing concentration (100, 50, and 20 pM) at a dose of 100 μL (this corresponds to an amount of 2.2×10^7, 1.1×10^7, and 0.55×10^7 AuNCs per gram of body weight, respectively) on the left forepaw pad of a rat, and then the left axillary region of the rat was noninvasively imaged using the PA system. The field of view that possibly contains SLN was chosen on the basis of our previous experience with lymph node imaging.[10,18,20] Before the injection of AuNCs, PA images were acquired as control images (Figure 3, A, D, and G), revealing the vasculature within ~3 mm below the skin surface. After the injection of AuNCs, a series of PA images were obtained up to 120 min postinjection. It can be observed that the SLNs started to appear at 5 min after the injection of 100 pM (Figure 3B) and 50 pM (Figure 3E) AuNC suspensions, while the SLN was not detected at 5 min after the injection of 20 pM AuNCs (Figure 3H). As time elapsed, the PA signals gradually increased and the SLNs, including the case with the injection of 20 pM AuNCs, could be clearly observed at 120 min postinjection (Figure 3, C, F, and I). Note that the minimum concentration of 20 pM we used here for PA SLN imaging in a rat model was about 100 times less than the value (2 nM) reported in our previous work,[18] greatly reducing the potential toxicity of AuNCs. It is also worth pointing out that the drainage of AuNCs to lymph nodes was much faster than that of Au nanorods, even at a relatively low injection concentration. In our previous study, it took more than 20 h for Au nanorods (10 nm in diameter and 41 nm in length) with an injection concentration of 1 μM to be observed at SLNs.[21] These results suggest that AuNCs should serve as a better diagnostic imaging agent than Au nanorods for SLN imaging.

We also performed *in vivo* PA SLN imaging in two additional rats at each concentration, following the same procedure. The PA signal enhancements in SLNs were summarized as a function of time (Figure 4A). Each data point was normalized against the PA signal from the corresponding adjacent blood vessels (BV) acquired before the injection of AuNCs. This normalization method was also applied to the experiments described in other sections. We found that the PA signal enhancement increased with increasing injection concentration. The enhancement also increased with postinjection time, indicating the gradual accumulation of AuNCs in SLNs. For example, after the

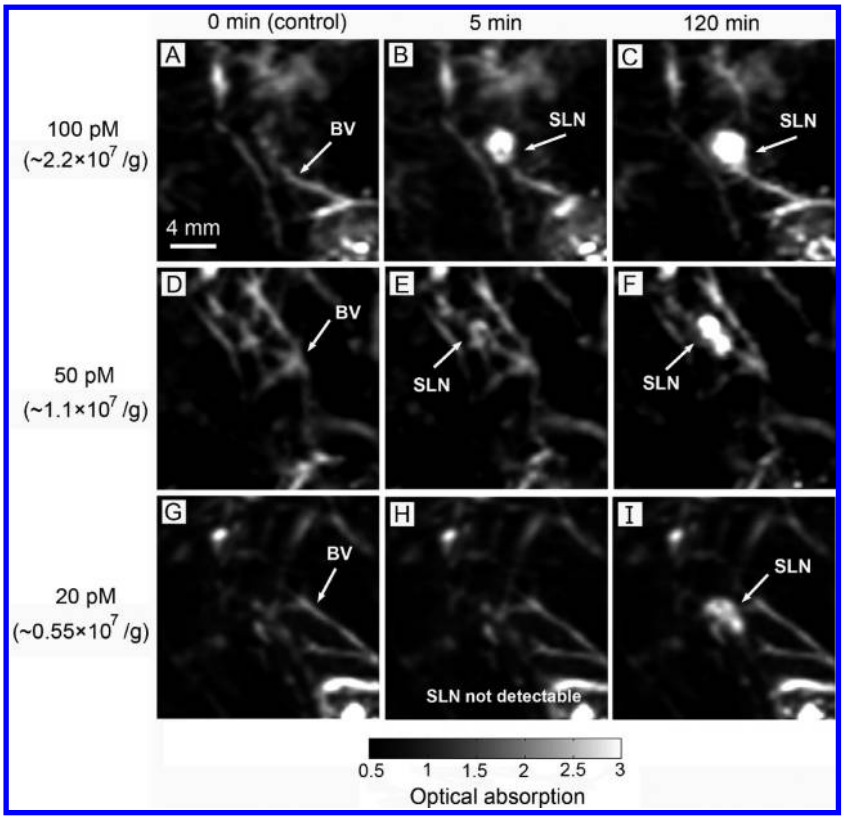

Figure 3. PA images of the axillary region of rats acquired at 0, 5, and 120 min after injection of the AuNCs with different concentrations. (A, D, G) PA images before injection of the AuNCs; (B, E, H) PA images 5 min after the injection of AuNCs at different concentrations. The SLNs started to appear except for the 20 pM sample; (C, F, I) PA images 120 min after the injection of AuNCs at different concentrations. The three concentrations correspond to amounts of 2.2×10^7, 1.1×10^7, and 0.55×10^7 AuNCs per gram of body weight, respectively. BV, blood vessels; SLN, sentinel lymph node.

injection of 100 pM AuNCs, the enhancement was 182% ± 12% at t = 5 min and then gradually increased to 355% ± 24% at t = 120 min postinjection. For the group with 20 pM AuNCs, the SLNs in two of the three rats were not even detected at t = 120 min postinjection. This high false negative rate indicates that we had reached the *in vivo* detection limit of the PA system. Note that the standard errors for PA signal enhancement at 5 and 30 min postinjection in the group of 50 pM AuNCs injection were still relatively high compared to those with the 100 pM sample, indicating that a 100 pM suspension of AuNCs at a dose of 100 μL (2.2×10^7 AuNCs per gram of body weight) seems to be the best candidate to start with for SLN imaging. We further quantified the number of AuNCs accumulated in the SLN by ICP-MS analysis of the excised node. The accumulated amount of AuNCs in SLN for the 100 pM sample was approximately 2 and 7.5 times higher than the 50 and 20 pM samples, respectively (Figure 4B). The average numbers of AuNCs in SLN per mass at 120 min postinjection of 20, 50, and 100 pM AuNCs were about $(0.86 \pm 0.74) \times 10^{10}$, $(3.25 \pm 1.07) \times 10^{10}$, and $(6.43 \pm 0.94) \times 10^{10}$ AuNCs/g, respectively, which were qualitatively consistent with the trend revealed by PA enhancement shown in Figure 4A. According to our measurements, about 18% of the injected 50 and 100 pM AuNCs had been accumulated in the SLN at t = 120 min postinjection, while about 12% of the injected 20 pM AuNCs had been accumulated in the SLN. On the basis of the ICP-MS data, there were about twice as many AuNCs in the SLN for the 100 pM sample than for the 50 pM sample, while the PA signal enhancement for the 100 pM sample showed only a slight increase. This discrepancy can be attributed to two reasons: (i) the AuNCs were actually not evenly distributed in the SLN. This phenomenon was observed in our previous report on SLN imaging.[18] The edges of the SLN were found to contain more nanocages than the central portion of the SLN. Therefore, if some parts of the SLN contained a small amount of AuNCs that generated PA signals lower than the background, we would not be able to detect them; (ii) the PA signal is sensitive to the imaging depth. If some parts of the SLN were away from the focus and the PA signal from AuNCs was lower than the background, the signal could not be detected either.

The SLNs of rats are located ~2 mm below the skin surface. In humans, the mean depth of SLNs is ~12 mm underneath the skin.[18] Therefore, it is necessary to demonstrate the minimal dose of AuNCs at the clinical depth by using the same PA imaging modality. Here, we used chicken breast tissues as biological phantoms.

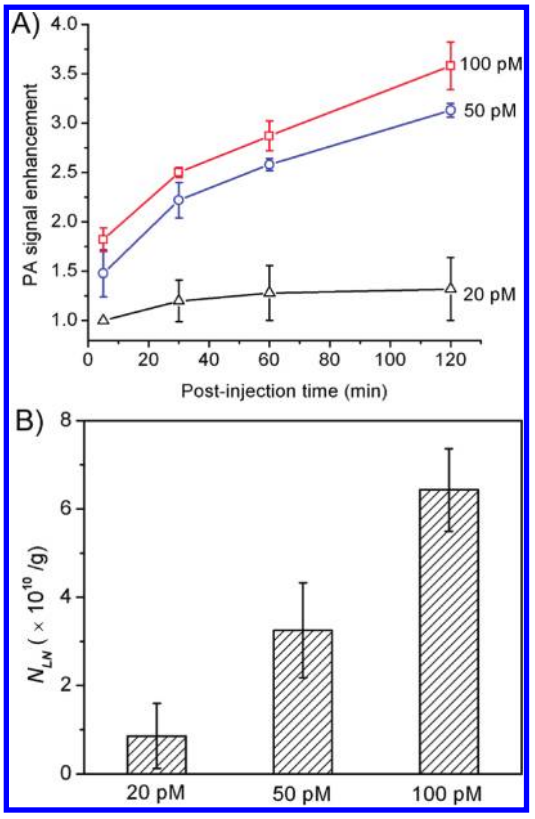

Figure 4. (A) PA signal enhancement in SLNs as a function of time after the injection of AuNCs at different concentrations (n = 3 rats for each group): 100, 50, and 20 pM, respectively. Each data point was normalized against the PA signal from the corresponding adjacent blood vessels before the injection of AuNCs. (B) Average numbers of AuNCs accumulated in the SLNs dissected at 120 min postinjection, as measured using ICP-MS. Here N_{LN} denotes the number of AuNCs per unit lymph node mass (g).

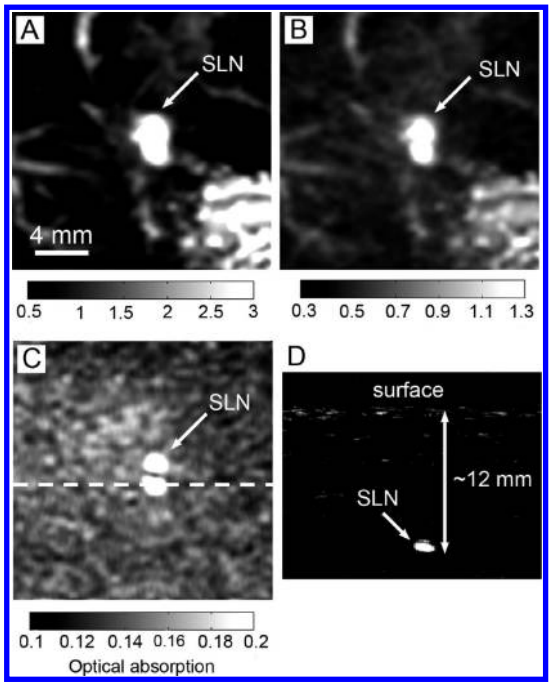

Figure 5. PA imaging of SLN in a rat after the injection of 100 pM AuNCs. The PA images were acquired (A) at 120 min postinjection with no chicken breast tissue added, (B) at 150 min postinjection with one layer (thickness: 5 mm) of chicken breast tissue added, and (C) at 180 min postinjection with two layers (total thickness: 10 mm) of chicken breast tissue added. (D) PA B-scan along the dashed line in (C), showing the SLN located at a depth of ~12 mm. SLN, sentinel lymph node.

The previously reported penetration depth for 1/e decay in chicken breast tissue was ~0.94 cm at a wavelength of 760 nm,[22] while the 1/e penetration depth at 785 nm in human breast was measured to be ~0.89 cm.[23] Similar to the previous experiments, after the SLN of a rat in the group of 100 pM AuNCs was identified (Figure 5A), a chicken breast tissue of 5 mm thick was placed on top of the axillary surface of the rat, and a PA image was acquired at 150 min postinjection. The SLN of the rat could be obviously identified from this image, and the total depth of the SLN was now ~7 mm (Figure 5B). With the addition of a second layer of chicken breast tissue, an imaging depth of ~12 mm was achieved by acquiring a PA image at 180 min postinjection (Figure 5C), and the SLN can still be imaged with a good contrast. In the B-scan image (Figure 5D), the depth information of the SLN is clearly shown with ~7 dB SNR.

An ideal mapping agent for lymphoscintigraphy should have proper size: on one hand, it should be small enough to rapidly drain to lymphatic vessels and then transport to lymph nodes; on the other hand, it should be large enough to stay within the lymph nodes during the imaging process. Particles smaller than 5 nm could easily leak into blood capillaries or migrate to echelon lymph nodes and thus cause false positives,[24] while particles larger than 100 nm are believed to be trapped in the interstitial compartment for a long period of time and are thus unable to transport to lymph nodes fast enough for lymphoscintigraphy.[25] Therefore, it is critical to identify an optimal size range for the AuNCs in order to have sufficiently fast migration and sufficient duration of trapping for SLN imaging.

We compared the PA enhancements in SLNs as a function of time using AuNCs with edge lengths of 50 and 30 nm, respectively (Figure 6A). We performed the *in vivo* PA imaging in three rats for each group. Note that the surface of the as-prepared AuNCs was covered with PVP, and thus the hydrodynamic diameter of the AuNCs measured by dynamic light scattering (DLS) was about 97.1 nm, so we did not choose AuNCs with an edge length larger than 50 nm. Additionally, nanoparticles with larger size (>50 nm) are known to exhibit short circulation times in blood,[26] making them less useful in diagnostic imaging. The injection concentrations for both the 30 nm and 50 nm AuNCs were 200 pM (at a dose of 100 μL), as the SLN could hardly be detected with the injection of 30 nm AuNCs at a concentration of 100 pM. The amounts of Au injected for 30 and 50 nm AuNCs were calculated to be about

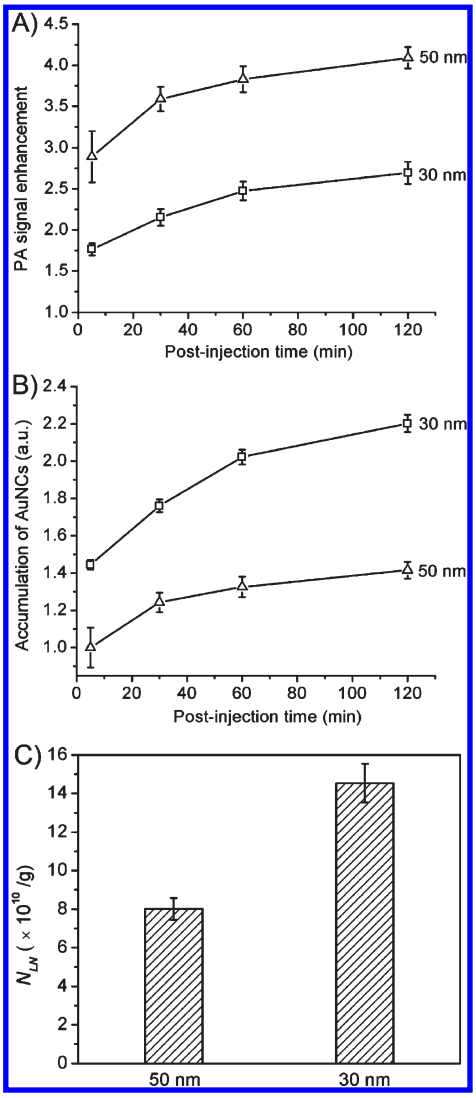

Figure 6. (A) PA signal enhancement in SLNs after the injection of 50 and 30 nm AuNCs with the same concentration and dose (200 pM and 100 μL) as a function of postinjection time (n = 3 rats for each group), respectively. (B) Accumulation of the 50 and 30 nm AuNCs in SLNs as a function of postinjection time calculated on the basis of the PA signals. The data points were normalized against the 50 nm AuNCs at 5 min postinjection. (C) Average numbers of AuNCs accumulated in the SLNs dissected at 2 h postinjection of the 30 and 50 nm AuNCs, as measured by ICP-MS. Here N_{LN} denotes the number of AuNCs per unit lymph node mass (g).

7.5 and 22.7 ng per gram of body weight, respectively. Both curves show that SLNs could be detected at 5 min postinjection, and the PA signal enhancement kept increasing in the following 120 min. It can be seen that the 50 nm AuNCs showed higher signal enhancement (about 150% to 170%) than the 30 nm sample. This difference can be ascribed to the fact that the 30 nm AuNCs had a smaller optical absorption cross section than the 50 nm AuNCs, generating weaker PA signals. We have also measured the absorption cross sections of these AuNCs using a PA-based method developed in our groups.[16] The absorption cross section of the 50 nm AuNCs at 760 nm was found to be about 2.1 times higher than that of the 30 nm AuNCs at 730 nm. Figure 6B shows a comparison of the accumulation of 50 and 30 nm AuNCs in SLNs as a function of post-injection time calculated from the PA signals. Since the PA signal is directly proportional to the absorption coefficient (μ_a) of the AuNCs,[16] the accumulation of AuNCs can be calculated according to the equation $N_{nano} = \mu_{a,nano}/\sigma_{a,nano}$, where N_{nano} is the concentration of the AuNCs (number of particles per m^3) and $\sigma_{a,nano}$ is the absorption cross section (m^2) of the nanocages. Each data point was then normalized against the accumulation of 50 nm AuNCs in SLN at 5 min post-injection. It can be seen that the 30 nm AuNCs transported into the SLN faster than the 50 nm AuNCs and showed a larger amount of accumulation in the SLN. The ICP-MS data in Figure 6C indicate that the average number of 30 nm AuNCs in the excised SLN per mass at 120 min postinjection was about 1.8 times higher than that of the 50 nm AuNCs, (14.5 ± 1.0) × 10^{10} *vs* (8.0 ± 0.6) × 10^{10} AuNCs/g, which is consistent with the trend of accumulation derived from the PA signals. The dose of Au accumulated in the SLN for 30 and 50 nm AuNCs at 120 min postinjection was about 2.5 × 10^{-5} and 4.1 × 10^{-5} g per gram of SLN, respectively. Even though the 30 nm AuNCs showed a larger amount of accumulation in SLN based on the particle number, the amount of Au content in SLN for the 50 nm AuNCs was about 1.6 times higher than that for the 30 nm AuNCs.

TABLE 1. Sumamry of the Hydrodynamic Diameters and Zeta-Potentials of the AuNCs Modified with Different Surface Groups

surface coating	hydrodynamic diameter (nm)	zeta-potentials (mV)
SH-PEG_{5000}- OMe	89.4 ± 3.7	−7.2 ± 4.2
SH-PEG_{5000}- NH_2	93.7 ± 4.5	+12.5 ± 1.5
SH-PEG_{5000}- COOH	92.0 ± 4.3	−16.8 ± 1.8

Early studies on the transport kinetics and lymphatic uptake of particles showed that surface characteristics, such as charge and hydrophobicity, could affect the rate of particle drainage from the injection site to lymph nodes and their distribution within the lymphatic system.[25] Therefore, it is important to study the transport behaviors of AuNCs with different surface charges. We replaced the PVP layer on the AuNCs with SH-PEG_{5000}-X (X = OMe, NH_2, or COOH). Table 1 summarized the hydrodynamic diameters and zeta-potentials of the PEGylated AuNCs. It can be observed that the zeta-potential of AuNCs covered with SH-PEG_{5000}-OMe was about −7.2 mV, and thus the surface charge is considered neutral. The zeta-potentials of AuNCs covered with SH-PEG_{5000}-NH_2 and SH-PEG_{5000}-COOH were around +12.5 and −16.8 mV, giving a relatively positive and negative surface charge, respectively. Following the same procedure, we performed *in vivo* SLN imaging using AuNCs modified with

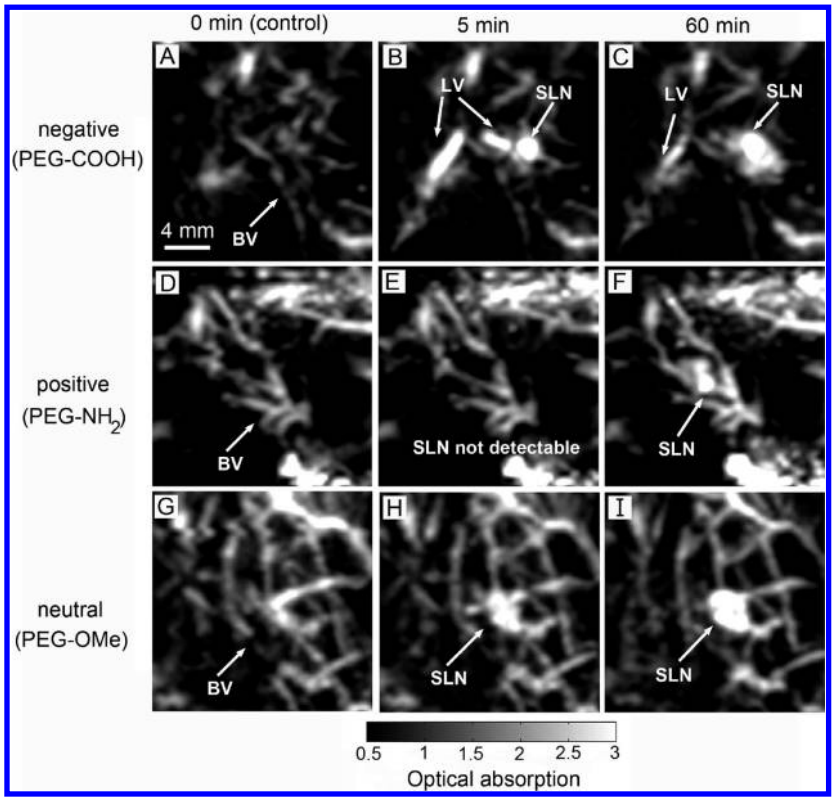

Figure 7. PA images acquired before and 5 and 60 min after the injection of AuNCs (200 pM, 100 μL) with different surface charges. The PVP layer on the nanocages surface was replaced with SH-PEG$_{5000}$-X, X = OMe, NH$_2$, or COOH, to generate a neutral, positive, or negative surface charge. (A, D, G) PA images before the injection of AuNCs: (B, E, H) PA images at 5 min postinjection of AuNCs with different charges. SLNs started to appear except for the case of AuNCs with positive charges. Some lymphatic vessels were also observed in the case of AuNCs with negative charges; (C, F, I) PA images at 60 min after the injection of AuNCs with different charges. BV, blood vessels; LV, lymphatic vessels; SLN, sentinel lymph node.

different surface charges. For comparison, each group had three rats and the injection concentration was 200 pM instead of 100 pM for all three groups, because the SLN could be hardly detected at 60 min after the injection of AuNCs with positive charges at a concentration of 100 pM. Figure 7 shows typical PA images acquired before as well as 5 and 60 min after the injection of AuNCs modified with different surface charges. Unlike the other two groups, AuNCs with negative charges accumulated not only in the SLN but also in the adjacent lymphatic vessels. The lymphatic vessels began to show up in PA images at 5 min postinjection (Figure 7B) and the AuNCs could be trapped there for 60 min (Figure 7C). It is known that lymphatic vessels play an important role in lymphatic metastasis,[27,28] providing crucial prognostic information. Cancer cells can exploit these vascular systems by expressing growth factors, altering the normal pattern of angiogenesis and lymphatic vessel growth, creating conduits for tumor metastasis. As a result, the ability to target and image aberrant drainage patterns is of clinical significance. However, studies on lymphatic vessels have been hindered by technical limitations.[29] The AuNCs with negative charges can potentially be used as a good contrast agent for lymphangiogenesis imaging. In addition, AuNCs with positive charges also showed a unique feature. It took 30 to 60 min, a much longer time than the other two groups, to transport to SLNs and accumulate enough for PA imaging (Figure 7, D−F). Figure 8A shows PA signal enhancement in SLNs as a function of time after the injection of AuNCs with different surface charges. It can be seen that the signal enhancement originating from AuNCs with positive charges is much lower than that from the neutral AuNCs, especially in the first 60 min postinjection, indicating a much slower transport rate to lymph nodes. As for the PA enhancement from the AuNCs with negative charges, it was also lower (about 50% to 60%) than the neutral AuNCs, but higher (about 150% to 160%) than the positive AuNCs in the first 60 min postinjection, and then leveled off. The ICP-MS data in Figure 8B show that the average number of AuNCs in the excised SLN per mass at 240 min postinjection decreased in the order of neutral > positive > negative, which is consistent with the trend for PA signal enhancement shown in Figure 8A.

We also found that the AuNCs were able to transport not only to the SLN but also further down to the second and third axillary lymph nodes of a rat. As shown in Figure 9, C and D, both *in vivo* and *ex vivo* PA images clearly show the accumulation of nanocages in all three lymph nodes of the rat after the injection of AuNCs at a

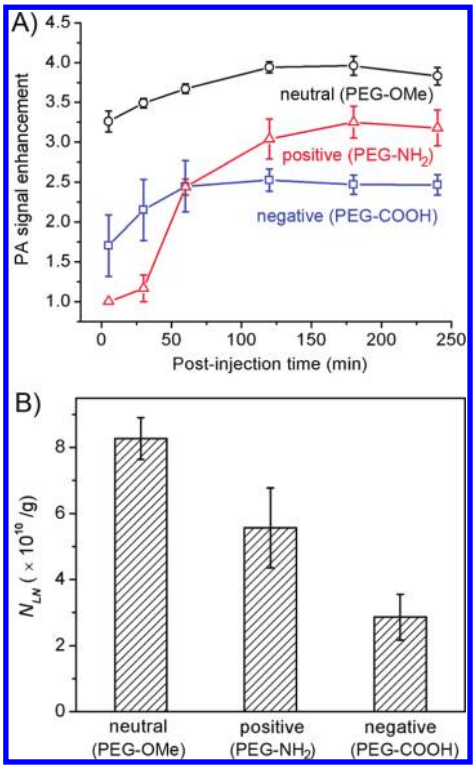

Figure 8. (A) PA signal enhancement in SLNs as a function of time postinjection of AuNCs with different surface charges: negative (blue line), positive (red line), and neutral (black line) (n = 3 rats for each group). (B) Average number of AuNCs accumulated in the SLN dissected at 4 h postinjection of AuNCs with different surface charges, as measured by ICP-MS (n = 3 rats for each group). Here N_{LN} denotes the number of AuNCs per unit lymph node mass (g).

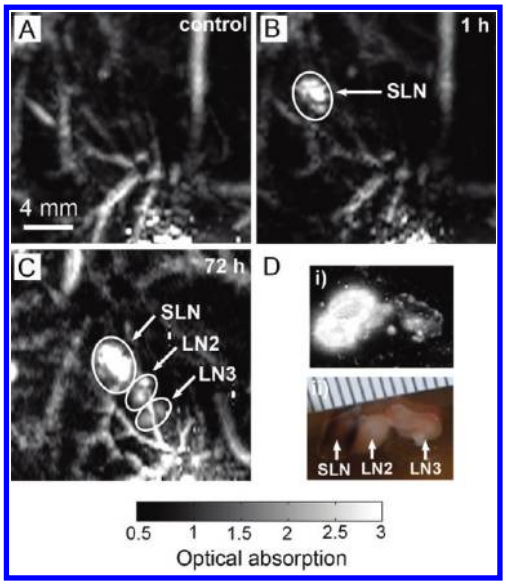

Figure 9. PA images acquired (A) before and (B) 1 h and (C) 72 h after the injection of AuNCs (500 pM, 100 μL), showing the transport of AuNCs from SLN to the second lymph node (LN2) and third lymph node (LN3). (D) *Ex vivo* (i) PA image and (ii) photograph of dissected lymph nodes containing AuNCs. The scale of the ruler is mm/div.

relatively higher concentration (500 pM) at 72 h postinjection (no transport to the second and third axillary lymph nodes had been observed by PA imaging after the injection of 100 or 200 pM nanocages). Taken together, these features can probably be used to design AuNCs with switchable surface charges for noninvasive axillary lymph node staging of breast cancer by taking advantage of their different transport kinetics in lymph nodes. For example, we can conjugate the surface of AuNCs with an enzyme-sensitive peptide, which can be cleaved by enzymes (*e.g.*, matrix metalloproteases, a recognized biomarker associated with cancer-cell invasion and metastasis) overexpressed by cancer cells in the metastatic lymph node.[30] As such, the surface charges on the AuNCs will be different before and after the enzyme cleavage, and the transport rates of AuNCs between lymph nodes will be different for patients with different stages of metastatic cancer. In addition, we can also attach fluorescence dyes to the surface of AuNCs *via* an enzyme-cleavable peptide.[31] The dye molecules will be cleaved and released from the surface of the nanocage in the presence of a protease, and thus fluorescence will be recovered. In practice, the distribution of AuNCs in lymph nodes can be mapped by PA imaging, while the protease activity can be monitored by fluorescence spectroscopy, providing critical information for the diagnosis of breast cancer metastasis. Related research is currently under way. With regard to the improvement for PA imaging, the system we used for this study employed a single ultrasonic transducer and a 10 Hz pulse-repetition-rate laser system, and thus the scanning time for a three-dimensional image was about 24 min with 0.2 and 0.4 mm step sizes. For future studies, employing an ultrasonic array system and a higher pulse-repetition-frequency laser system can dramatically improve the temporal resolution. We are currently developing a hand-held, array-based PA system for future clinical use.[32,33]

CONCLUSION

We have quantitatively evaluated the transport of AuNCs in a lymphatic system and their uptake by lymph nodes in a rat model through PA imaging. We systematically examined and optimized a number of experimental parameters including the concentration, size, and surface characteristics of the AuNCs. We reduced the concentration of injected AuNCs to 100 pM (20 times lower than our previous proof-of-concept report, greatly reducing the potential toxicity of AuNCs) for SLN imaging at a depth of ~12 mm (the depth of SLN in human) while keeping a sufficient SNR. It was found that the 30 nm AuNCs exhibited a faster transport rate and a larger amount of accumulation in the SLN than the 50 nm AuNCs, but the latter generated stronger PA signals due to a larger optical absorption cross section. This result indicates that the 50 nm AuNCs seem to be a better contrast agent than the 30 nm AuNCs for SLN imaging by PA tomography. As for AuNCs with different

surface charges, their transport rates to SLNs decreased in the order of neutral > negative > positive. In addition, AuNCs with negative charges could be trapped in lymphatic vessels, making them potentially useful as contrast agents for lymphangiogenesis by PA imaging. We also found that the AuNCs not only were able to transport to the SLN but can also travel farther to the second and third axillary lymph nodes of a rat. These results can serve as guidelines for choosing optimal experimental parameters of AuNCs in metastatic lymph nodes mapping and other biomedical applications by noninvasive PA imaging.

METHODS

Synthesis and Surface Modification of AuNCs. The AuNCs were synthesized using the galvanic replacement reaction between Ag nanocubes and chloroauric acid in water according to our published protocol.[34] In a typical synthesis, an aqueous solution of $HAuCl_4$ (0.75 mM) was slowly titrated (at a rate of 45 mL/h using a syringe pump) into an aqueous suspension of Ag nanocubes placed in a three-neck flask at 90 °C. The extent of replacement could be readily monitored by taking UV−vis spectra of aliquots sampled from the solution. To obtain different surface charges, the nanocages were derivatized with SH-PEG_{5000}-X (X = OMe, NH_2, and COOH; all from Laysan Bio; $M_w \approx 5000$). In a typical process, 0.1 mL of HS-PEG_{5000}-X aqueous solution (0.1 mM) and 0.1 mL of AuNCs aqueous suspension (1 nM in terms of particles) were added to 2.8 mL of deionized water. The mixture was kept stirring at 4 °C overnight. After that, the mixture was centrifuged at 14 000 rpm for 15 min, and the supernatant was decanted to remove the excess PEG. The PEGylated-AuNCs were then washed with water twice and resuspended in water at different concentrations of 200 pM (in terms of particles) for *in vivo* studies.

The PA Imaging System. A deep reflection-mode PA imaging system was used (Scheme 1 in ref 19) for all PA experiments. A tunable Ti:sapphire laser (LT-2211A; Lotis TII, Minsk, Belarus) pumped by a Q-switched Nd:YAG (LS-2137; Lotis TII) laser was used for excitation, providing a <15 ns pulse duration and a 10 Hz pulse repetition rate. A dark-field ring-shaped illumination was adopted to reduce the surface PA signal generation.[35] The light energy on the sample surface was controlled to be less than the American National Standards Institute standard for maximum permissible exposure. Two wavelengths, 760 and 730 nm, were used for PA imaging to match the absorption peak positions of the 50 and 30 nm AuNCs, respectively. A 5 MHz central frequency, spherically focused ultrasonic transducer (V308; Panametrics-NDT, Waltham, MA, USA) was used to acquire the generated PA signals. The 5 MHz ultrasonic transducer yields axial and transverse resolutions of 150 and 560 μm, respectively. The signal was amplified by a low-noise amplifier (5072PR; Panametrics-NDT) and recorded using a digital oscilloscope (TDS 5054, Tektronix, Beaverton, OR). A photodiode (SM05PD1A, Thorlabs, Newton, NJ, USA) was used to compensate for the energy instability of laser pulses. A linear translation stage (XY-6060, Danaher Motion, Radford, VA, USA) was used for raster scanning to obtain three-dimensional (3D) PA data. The signal was not averaged for any image to shorten the data acquisition time. By measuring PA amplitudes according to the arrival times, one-dimensional depth-resolved images (A-lines) are acquired. Additional raster scanning along a transverse direction provides two-dimensional depth-resolved images (B-scans), consisting of multiple A-scans, and further scanning along the other traverse direction provides 3D images. The acquired 3D raw data can be processed as a maximum amplitude projection (MAP)—a projection of the maximum PA amplitude along each A-line onto the corresponding plane. Typical scanning values were as follows: field of view, 20 × 20 mm; voxel dimension, 0.2 × 0.4 mm; laser pulse repetition rate, 10 Hz; and acquisition time, ~24 min. The transducer was located inside a water container with an opening of 5 × 5 cm at the bottom, sealed beneath a photoacoustically transparent clear membrane. The rats or gelatin phantom samples made from a mixture of gelatin solution and AuNCs were placed under the membrane, and ultrasonic gel was used for ultrasound coupling.

Animal Handling. All animal experiments were in compliance with the Washington University Institutional Animal Care and Use Committee. Sprague−Dawley rats weighting 250−300 g (Harlan, Indianapolis, IN, USA) were anesthetized with a mixture of ketamine (87 mg/kg) and xylazine (13 mg/kg) at a dose of 0.15 mL per 100 g body weight. The hair in the left axillary region was removed by gentle clipping and depilatory cream before imaging. PA imaging was acquired before and after intradermal injection of AuNC solution (0.1 mL) in the left forepaw pad. Full anesthesia of the animal was maintained throughout the experiment by using vaporized isoflurane (1 L/min of oxygen and 0.75% isoflurane), and vitals were monitored by a pulse oximeter (NOMIN Medical, 2000SA). The body temperatures of the rats were maintained with a water heating pad. After data acquisition, the rats were euthanized by overdosed pentobarbital, and SLNs were dissected for ICP-MS measurements.

ICP-MS of AuNCs in Dissected Lymph Nodes. The excised lymph nodes were weighed and then were completely digested with 5 mL of aqua regia in a 50 mL beaker at boiling temperature. The solution was evaporated to 1 mL and subsequently diluted to 15 mL with deionized water. Samples were passed through a 0.45 mm filter to remove any undigested debris prior to ICP-MS measurement. The analysis of Au content was performed with ICP-MS (Perkin-Elmer, Elan DRC II), and the concentration of Au ions was converted to the concentration of nanocages once the geometric dimensions of the nanocage had been determined from TEM images.

Conflict of Interest: L.V.W. has a financial interest in Microphotoacoustics, Inc. and Endra, Inc., which, however, did not support this work.

Acknowledgment. This work was supported in part by a 2006 NIH Director's Pioneer Award (DP1 OD000798), a grant from the NCI (R01 CA13852701), and startup funds from Washington University in St. Louis to X.Y. It was also sponsored by other NIH grants (R01 EB000712, R01 EB008085, R01 CA134539, and U54 CA136398) and a grant from St. Louis Institute for Nanomedicine (SLIN) to L.V.W. Part of the research was performed at the Nano Research Facility, a member of the National Nanotechnology Infrastructure Network (NNIN), which is supported by the NSF under ECS-0335765. Contact Y.X. for the synthesis and surface modification of gold nanocages and L.V.W. for photoacoustic imaging.

REFERENCES AND NOTES

1. Alazraki, N. P.; Eshima, D.; Eshima, L. A; Herda, S. C.; Murray, D. R.; Vansant, J. P.; Taylor, A. T. The Sentinel Node Concept, and the Intraoperative Gamma Probe in Melanoma, Breast Cancer, and Other Potential Cancers. *Semin. Nucl. Med.* **1997**, *27*, 55–67.
2. Kobayashi, H.; Kawamoto, S.; Sakai, Y.; Choyke, P. L.; Star, R. A.; Brechbiel, M. W.; Sato, N.; Tagaya, Y.; Morris, J. C.; Waldmann, T. A. Lymphatic Drainage Imaging of Breast Cancer in Mice by Micro-Magnetic Resonance Lymphangiography Using a Nano-Size Paramagnetic Contrast Agent. *J. Natl. Cancer Inst.* **2004**, *96*, 703–708.
3. Amersi, F.; Hansen, N. M. The Benefits and Limitations of Sentinel Lymph Node Biopsy. *Curr. Treat. Options Oncol.* **2006**, *7*, 141–151.

4. McMasters, K. M.; Tuttle, T. M.; Carlson, D. J.; Brown, C. M.; Noyes, R. D.; Glaser, R. L.; Vennekotter, D. J.; Turk, P. S.; Tate, P. S.; Sardi, A.; *et al*. Sentinel Lymph Node Biopsy for Breast Cancer: a Suitable Alternative to Routine Axillary Dissection in Multi-Institutional Practice when Optimal Technique Is Used. *J. Clin. Oncol.* **2000**, *18*, 2560–2566.
5. Purushotham, A. D.; Upponi, S.; Klevesath, M. B.; Bobrow, L.; Millar, K.; Myles, J. P.; Duffy., S. W. Morbidity after Sentinel Lymph Node Biopsy in Primary Breast Cancer: Results from a Randomized Controlled Trial. *J. Clin. Oncol.* **2005**, *23*, 4312–4321.
6. Krishnamurthy, S.; Sneige, N.; Bedi, D. G.; Edieken, B. S.; Fornage, B. D.; Kuerer, H. M.; Singletary, S. E.; Hunt, K. K. Role of Ultrasound-Guided Fine-Needle Aspiration of Indeterminate and Suspicious Axillary Lymph Nodes in the Initial Staging of Breast Carcinoma. *Cancer* **2002**, *95*, 982–988.
7. Wang, L. V. Multiscale Photoacoustic Microscopy and Computed Tomography. *Nat. Photonics* **2009**, *3*, 503–509.
8. Kim, C.; Favazza, C.; Wang, L. V. *In Vivo* Photoacoustic Tomography of Chemicals: High-Resolution Functional and Molecular Optical Imaging at New Depths. *Chem. Rev.* **2010**, *110*, 2756–2782.
9. Ku, G.; Wang, L. V. Deeply Penetrating Photoacoustic Tomography in Biological Tissues Enhanced with an Optical Contrast Agent. *Opt. Lett.* **2005**, *30*, 507–509.
10. Song, K. H.; Stein, E. W.; Margenthaler, J. A.; Wang, L. V. Noninvasive Photoacoustic Identification of Sentinel Lymph Nodes Containing Methylene Blue *In Vivo* in a Rat Model. *J. Biomed. Opt.* **2008**, *13*, 054033-1–054033-6.
11. Kim, C.; Song, K. H.; Gao, F.; Wang, L. V. Sentinel Lymph Nodes and Lymphatic Vessels: Noninvasive Dual-Modality *In Vivo* Mapping by Using Indocyanine Green in Rats—Volumetric Spectroscopic Photoacoustic Imaging and Planar Fluorescence Imaging. *Radiology* **2010**, *255*, 442–450.
12. Sohrabnezhad, S.; Pourahmad, A.; Sadjadi, M. A. New Methylene Blue Incorporated in Mordenite Zeolite as Humidity Sensor Material. *Mater. Lett.* **2007**, *61*, 2311–2314.
13. Skrabalak, S. E.; Chen, J; Sun, Y; Lu, X; Au, L; Cobley, C; Xia, Y. Gold Nanocages: Synthesis, Properties, and Applications. *Acc. Chem. Res.* **2008**, *41*, 1587–1595.
14. Chen, J.; Saeki, F.; Wiley, B. J.; Cang, H.; Cobb, M. J.; Li, Z. Y.; Au, L.; Zhang, H.; Kimmey, M. B.; Li, X.; *et al.* Gold Nanocages: Bioconjugation and Their Potential Use as Optical Imaging Contrast Agents. *Nano Lett.* **2005**, *5*, 473–477.
15. Kim, C.; Cho, E. C.; Chen, J.; Song, K. H.; Au, L.; Favazza, C.; Zhang, Q.; Cobley, C. M.; Gao, F.; Xia, Y.; *et al. In Vivo* Molecular Photoacoustic Tomography of Melanomas Targeted by Bioconjugated Gold Nanocages. *ACS Nano* **2010**, *4*, 4559–4564.
16. Cho, E. C.; Kim, C.; Zhou, F.; Cobley, C. M.; Song, K. H.; Chen, J.; Li, Z.; Wang, L. V.; Xia, Y. Measuring the Optical Absorption Cross Sections of Au−Ag Nanocages and Au Nanorods by Photoacoustic Imaging. *J. Phys. Chem. C* **2009**, *113*, 9023–9028.
17. Chen, J.; Yang, M.; Zhang, Q.; Cho, E. C.; Cobley, C. M.; Claus, C.; Kim, C.; Wang, L. V.; Welch, M. J.; Xia, Y. Gold Nanocages: a Novel Class of Multifunctional Nanomaterials for Theranostic Applications. *Adv. Funct. Mater.* **2010**, *20*, 3684–3694.
18. Song, K. H.; Kim, C.; Cobley, C. M.; Xia, Y.; Wang, L. V. Near-Infrared Gold Nanocages as a New Class of Tracers for Photoacoustic Sentinel Lymph Node Mapping on a Rat Model. *Nano Lett.* **2009**, *9*, 183–188.
19. Song, K. H.; Wang, L. V. Deep Reflection-Mode Photoacoustic Imaging of Biological Tissue. *J. Biomed. Opt.* **2007**, *12*, 060503-1–060503-3.
20. Kim, C.; Song, K. H.; Gao, F.; Wang, L. V. Sentinel Lymph Nodes and Lymphatic Vessels: Noninvasive Dual-Modality In Vivo Mapping by Using Indocyanine Green in Rats—Volumetric Spectroscopic Photoacoustic Imaging and Planar Fluorescence Imaging,. *Radiology* **2010**, *255*, 442–450.
21. Song, K. H.; Kim, C.; Maslov, K.; Wang, L. V. Noninvasive *in Vivo* Spectroscopic Nanorod-Contrast Photoacoustic Mapping of Sentinel Lymph Nodes. *Eur. J. Radiol.* **2009**, *70*, 227–231.
22. Marquez, G.; Wang, L. V.; Lin, S. P.; Schwartz, J. A.; Thomsen, S. L. Anisotropy in the Absorption and Scattering Spectra of Chicken Breast Tissue. *Appl. Opt.* **1998**, *37*, 798–804.
23. Spinelli, L.; Torricelli, A.; Pifferi, A.; Taroni, P.; Danesini, G. M.; Cubeddu, R. Bulk Optical Properties and Tissue Components in the Female Breast from Multiwavelength Time-Resolved Optical Mammography. *J. Biomed. Opt.* **2004**, *9*, 1137–1142.
24. Soltesz, E. G.; Kim, S.; Laurence, R. G.; DeGrand, A. M.; Parungo, C. P.; Dor, D. M.; Cohn, L. H.; Bawendi, M. G.; Frangioni, J. V.; Mihaljevic, T. Intraoperative Sentinel Lymph Node Mapping of the Lung Using Near-Infrared Fluorescent Quantum Dots. *Ann. Thorac. Surg.* **2005**, *79*, 269–277.
25. Moghimi, S. M.; Rajabi-siahboomi, A. R. Advanced Colloid-Based Systems for Efficient Delivery of Drugs and Diagnostic Agents to the Lymphatic Tissues. *Prog. Biophys. Mol. Biol.* **1996**, *65*, 221–249.
26. Zhang, G.; Yang, Z.; Lu, W.; Zhang, R.; Huang, Q.; Tian, M.; Li, L.; Liang, D.; Li, C. Influence of Anchoring Ligands and Particle Size on the Colloidal Stability and *in Vivo* Biodistribution of Polyethylene Glycol-Coated Gold Nanoparticles in Tumor-Xenografted Mice. *Biomaterials* **2009**, *30*, 1928–1936.
27. Padera, T. P.; Kadambi, A.; di Tomaso, E.; Carreira, C. M.; Brown, E. B.; Boucher, Y.; Choi, N. C.; Mathisen, D.; Wain, J.; Mark, E. J.; *et al.* Lymphatic Metastasis in the Absence of Functional Intratumor Lymphatics. *Science* **2002**, *296*, 1883–1886.
28. Kwon, S.; Sevick-Muraca, E. M. Noninvasive Quantitative Imaging of Lymph Function in Mice. *Lymphat. Res. Biol.* **2007**, *5*, 219–231.
29. Shayan, R.; Achen, M. G.; Stacker, S. A. Lymphatic Vessels in Cancer Metastasis: Bridging the Gaps. *Carcinogenesis* **2006**, *27*, 1729–1738.
30. Stamenkovic, I. Matrix Metalloproteinases in Tumor Invasion and Metastasis. *Semin. Cancer Biol.* **2000**, *10*, 415–433.
31. Xia, X.; Yang, M.; Oetjen, L. K.; Zhang, Y.; Li, Q.; Chen., J.; Xia, Y. An Enzyme-Sensitive Probe for Photoacoustic Imaging and Fluorescence Detection of Protease Activity. *Nanoscale* **2011**, *3*, 950–953.
32. Erpelding, T. N.; Kim, C.; Pramanik, M.; Jankovic, L.; Maslov, K.; Guo, Z.; Margenthaler, J. A.; Pashley, M. D.; Wang, L. V. Sentinel Lymph Nodes in the Rat: Noninvasive Photoacoustic and US Imaging with a Clinical US System. *Radiology* **2010**, *256*, 102–110.
33. Kim, C.; Erpelding, T. N.; Maslov, K.; Jankovic, L.; Akers, W. J.; Song, L.; Achilefu, S.; Margenthaler, J. A.; Pashley, M. D.; Wang, L. V. Handheld Array-Based Photoacoustic Probe for Guiding Needle Biopsy of Sentinel Lymph Nodes. *J. Biomed. Opt.* **2010**, *15*, 046010.
34. Zhang, Q.; Li, W.; Wen, L. P.; Chen, J.; Xia, Y. Facile Synthesis of Ag Nanocubes of 30 to 70 nm in Edge Length with CF_3COOAg as a Precursor. *Chem.—Eur. J.* **2010**, *16*, 10234–10239.
35. Maslov, K.; Stoica, G.; Wang, L. V. *In Vivo* Dark-Field Reflection-Mode Photoacoustic Microscopy. *Opt. Lett.* **2005**, *30*, 625–627.